Design Optimization for Automated Fibre Placement Manufacturing of Linerless Hydrogen Composite Pressure Vessels

M. Lanzo[1*], P. Shabani[1], L. Li[2], and J. Laliberte[1]

[1] Department of Mechanical and Aerospace Engineering, Carleton University, Ottawa, Canada
[2] Aerospace Research Centre, National Research Council Canada, Ottawa, Canada

* *Corresponding author (melinalanzo@cmail.carleton.ca)*

Keywords: *Composite Materials; Hydrogen Storage; Automated Fibre Placement; Finite Element Analysis; Composite Pressure Vessel*

1. Abstract

Hydrogen presents a promising pathway for clean energy in the transportation sector, offering an onboard fuel option that produces zero carbon emissions during operation. A key challenge to its widespread adoption lies in the efficient and safe storage of hydrogen. Linerless composite pressure vessels, classified as Type V structures, represent one such solution, with the potential for significant weight reduction and increased internal storage volume compared to Type I–IV tanks. To further enhance vessel performance beyond the constraints of traditional manufacturing, automated fibre placement (AFP) presents a compelling alternative to filament winding. Through its tow-cutting and fibre-steering capabilities, AFP enables discontinuous non-geodesic layups, reducing redundant material and expanding the design space through spatial variations of fibre angles along the dome contour.

In this study, an automated design-to-analysis tool was developed. In Python, design optimization followed a dual approach: a continuous ply-drop algorithm optimized thickness to match the ideal isotensoid thickness profile, while fibre angles were optimized based on non-geodesic winding. The development of a finite element model in Abaqus was automated using scripting and executed with a Fortran user-material subroutine to model composite material behaviour and capture spatially varying fibre angles along the dome contour. The FEA was performed to identify a suitable design capable of withstanding an internal pressure of 20 MPa. The Hashin failure criteria were employed to predict fibre and matrix failures and ensure both the structural integrity and sealing of the linerless design. The results demonstrate the performance-driven design opportunities enabled by AFP manufacturing.

2. Introduction

As industries seek alternative energy carriers to achieve net-zero greenhouse gas emissions by 2050, hydrogen has emerged as a leading candidate to support decarbonizing the transportation sector. Hydrogen can be converted to electricity in fuel cells or combusted directly in engines, producing no carbon emissions at the point of use and offering the potential for sustainable production from renewable energy sources [1]. Although hydrogen has a superior gravimetric energy density compared with conventional vehicle fuels, its low volumetric energy density presents a significant challenge for onboard storage. To increase its volumetric density, hydrogen must be stored under extreme conditions, including high-pressure compression, cryogenic liquefaction, or cryo-compressed storage [1]. As such, the development of safe and efficient storage systems remains a critical step toward the widespread adoption of hydrogen technologies.

To address this challenge, five classes of hydrogen storage vessels have been developed, ranging from all-metal Type I tanks to linerless all-composite Type V tanks, with Types II–IV employing varying combinations of metal or polymer liners and composite reinforcement. Linerless composite pressure vessels, classified as Type V structures, represent the most recent development and offer the potential for significant weight reduction and increased internal storage volume compared with Types I–IV [2]. These benefits are particularly valuable in weight-sensitive industries like automotive and aerospace. In addition, Type V tanks provide important safety advantages, including the elimination of liner collapse risks and the promotion of the desirable leak-before-burst failure mode.

Automated fibre placement (AFP) offers a promising alternative to conventional filament winding (FW) by overcoming several of its manufacturing limitations in composite vessel production [2]. In FW, fibres are deposited as continuous tows, which can lead to localized redundant thicknesses. Moreover, fibres tend to follow geodesic paths, defined as the shortest path connecting two points on a surface, while deviation from this path is restricted by surface friction. This restricts the realization of non-geodesic fibre placement geometries, which may improve structural performance [3-6]. In contrast, AFP can cut, restart, and steer individual tows. These capabilities allow for localized adjustments that reduce unnecessary material accumulation and expand the design envelope, enabling new potentials for structural optimization and weight reduction.

Prior research has demonstrated the potential of AFP in pressure vessel manufacturing. A US Department of Energy-funded project employed a hybrid manufacturing approach for 70 MPa Type IV tanks, applying AFP to reinforce the dome regions and FW to construct the cylindrical section and overwrap the entire vessel [7]. The 129 L hybrid vessel achieved 32% reduction in composite mass and 20% reduction in cost compared to the fully FW vessel. Similarly, the NASA-Boeing Composite Cryotank Technologies and Demonstration Project utilized AFP to build 2.4 m and 5.5 m diameter Type V tanks [8]. Compared to the baseline aluminum-lithium tanks, the AFP tanks achieved approximately 25% weight savings and 30% cost reduction.

To investigate the potential advantages of AFP manufacturing for Type V pressure vessels, a manufacturing-informed numerical design framework is required to accurately capture localized thickness buildup and fibre angle variations along the dome. Analytical models for filament winding have been widely explored in the literature [4, 9-12], and these formulations have been adapted to AFP by Air et al. [5]. Building on this manufacturing physics framework, Air et al. [5] explored structural design optimization by employing: 1) cutting and continuous ply-drop algorithms to match the ideal isotensoid geodesic thickness profile, and 2) non-geodesic trajectories to tailor local fibre angles. For thickness minimization, plies can be cut or redirected at specific radial locations, referred to as drop radii, where the local thickness exceeds the ideal profile. The cut method terminates and restarts plies at the drop radius, whereas the continuous method steers bands tangent to the drop radius. Based on its reduced defects and improved leakage resistance under experimental testing, Air et al. [5] focused their optimization on the continuous steering approach. Accordingly, the continuous method was implemented in the present study.

This work develops an automated design-to-analysis framework that operates through three interconnected modules. First, a Python-based design code calculates the tank geometry and winding trajectories governed by manufacturing physics. Second, a Python script interfacing with Abaqus generates an axisymmetric finite element model for burst testing. Finally, a custom Fortran user-material (UMAT) subroutine is executed during the finite element analysis (FEA) to evaluate ply-level failure criteria while accounting for spatially varying material orientations along the dome. The utility of the design tool was demonstrated through the design and analysis of a 20 MPa composite vessel.

3. Numerical modelling framework

3.1. Fibre placement manufacturing physics

For composite pressure vessels, an isotensoid dome shape is often considered ideal for achieving theoretically uniform stress along the fibre direction [13]. This dome shape can be defined by its meridian profile as shown in Figure 1, where r is the radial coordinate, z is the axial coordinate, r_0 is the polar boss opening radius, r_f is the polar boss contact radius, and R is the equatorial radius [10, 12]. At each radial coordinate, the fibre angle, φ, and the surface normal angle relative to the z-axis, θ, are defined. The fibre angle approaches 90° at r_0 to maintain tangency with the polar opening [5]. Finally, the cylindrical section is characterized by its half-length L_c.

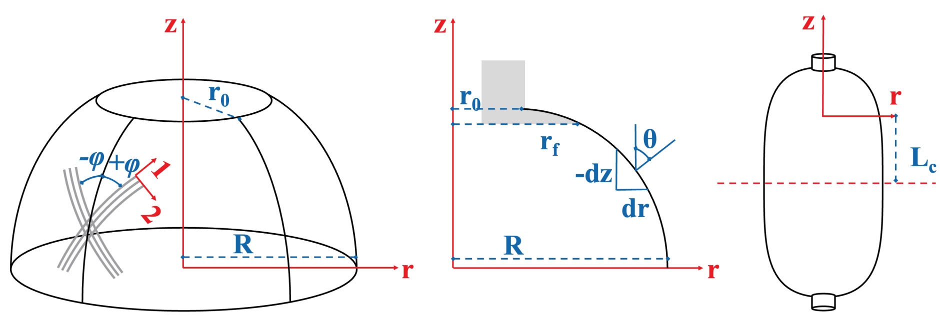

Figure 1. Isotensoid meridian profile, adapted from [12].

The ideal thickness profile for a geodesic isotensoid dome can be defined by Equation 1, where the equatorial thickness is given by $h_R = 2nt$, with t representing the ply thickness and n representing the number of $\pm\varphi$ plies [10, 12]. This ideal thickness profile provides the basis for design optimization by selectively steering plies at specific radial locations.

$$h_{ideal}(r) = h_R \frac{R\cos(\varphi_R)}{r\cos(\varphi)} \tag{1}$$

Mathematical models have been developed and experimentally validated in the literature to define the isotensoid meridian profile for both geodesic and non-geodesic trajectories [4, 5, 9-12]. The degree of slippage is characterized by the coefficient, λ, where $\lambda = 0$ corresponds to a geodesic path. The isotensoid dome geometry and fibre angle are coupled and can be obtained by solving the initial value problem defined by Equations 2 and 3 [4, 5]. The initial conditions at $r = r_0$ are $\varphi_0 = \pi/2$, $z_0 = 0$, and $z'_0 = 0$, where the choice of z_0 is arbitrary and only affects the position of the dome along the z-axis. The fibre force constant, S, is selected such that a solution exists over the entire interval $[r_0, R]$ while maximizing z'_R to uphold continuity of the profile at the cylinder-dome junction. In this work, the optimal value of S was determined using a two-stage search strategy, consisting of an initial coarse scan followed by a golden section search, to improve computational efficiency.

$$z'' = \frac{\left(1+z'^2\right)\left(Sz'tan^2(\varphi)\sqrt{1+\lambda^2} + 2r^2 sec\,(\varphi)\sqrt{1+z'^2}\right)}{Sr\sqrt{1+\lambda^2}} \tag{2}$$

$$\frac{d\varphi}{dr} = -\frac{tan(\varphi)}{r} - \frac{2\lambda r\sqrt{1+z'^2}}{S\sqrt{1+\lambda^2}} \tag{3}$$

The corresponding thickness distribution in isotensoid domes can also be described using established analytical models [4, 5, 9-12]. For non-geodesic winding, Equation 4 can be used as an approximation of the actual manufactured thickness, where w is the fibre bandwidth and $N = 2\pi R cos(\varphi_R)/w$ is the number of roving bands for a single ply. Air et al. [5] introduced a correction factor to adapt this expression from geodesic to non-geodesic winding. The correction factor modifies Δ such that the effective bandwidth linearly decreases to zero between three bandwidths from the polar opening and the equator. The radial position at k fibre bandwidths from the polar opening, r_{kw}, can be determined using its exact arc length calculation, as shown by Equation 5.

$$h(r) = \begin{cases} \dfrac{\sqrt{1+z'^2}Nt}{2\pi}\left(\dfrac{\pi}{2} - \varphi\right), & r_0 < r \le r_w \\ \dfrac{Nwt}{2\pi r cos(\varphi)}\left(1 + \dfrac{sin\,(\varphi)}{cos^2(\varphi)}\cdot\dfrac{\Delta}{2!} + \dfrac{1+2sin^2(\varphi)}{cos^4(\varphi)}\cdot\dfrac{\Delta^2}{3!} + \cdots\right), & r_w < r \le R\,, \end{cases} \tag{4}$$

$$\Delta = \left(w\sqrt{1+z'^2}\right)/r$$

$$k\cdot w = \int_{r_0}^{r_{kw}} \sqrt{1+z'^2}dr \tag{5}$$

To smooth the non-physical thickness peak within two bandwidths of the polar opening, a cubic spline approximation $h_a(r)$ is implemented following Equation 6 [10]. The polynomial coefficients are determined by solving a linear system governed by four distinct constraints: C^0 and C^0 continuity at r_{2w}, a boundary thickness match at the polar opening $h_a(r_0) = t$, and a total material volume conservation across the interval $[r_0, r_{2w}]$.

$$h_a(r) = a_0 + a_1 r + a_2 r^2 + a_3 r^3, \qquad r_0 \le r \le r_{2w} \tag{6}$$

3.2. Design-to-analysis computational framework

The design optimization framework consists of three coupled components, as illustrated in Figure 2. First, a Python design code computes the full tank geometry based on the manufacturing physics defined above. Thickness is optimized based on the continuous ply drop algorithm developed in [5]. As each ply is added iteratively, if the cumulative thickness exceeds the ideal thickness, the corresponding radial location is determined, and a steered full ply is introduced in place of a standard full ply. The geometry, winding angle, and thickness are then recalculated with $r_0 = r_{drop}$ to define the steered ply. This loop is repeated until the full layup is built, after which the code outputs the composite shell and boss geometry, a φ–θ orientation map, and Abaqus node sets. Together, φ and θ account for both the winding trajectory and the dome curvature, establishing the local material orientation. The Abaqus node sets are used to define the ply layer and normal partitions, the boss-composite contact interface, and the internal pressure surfaces.

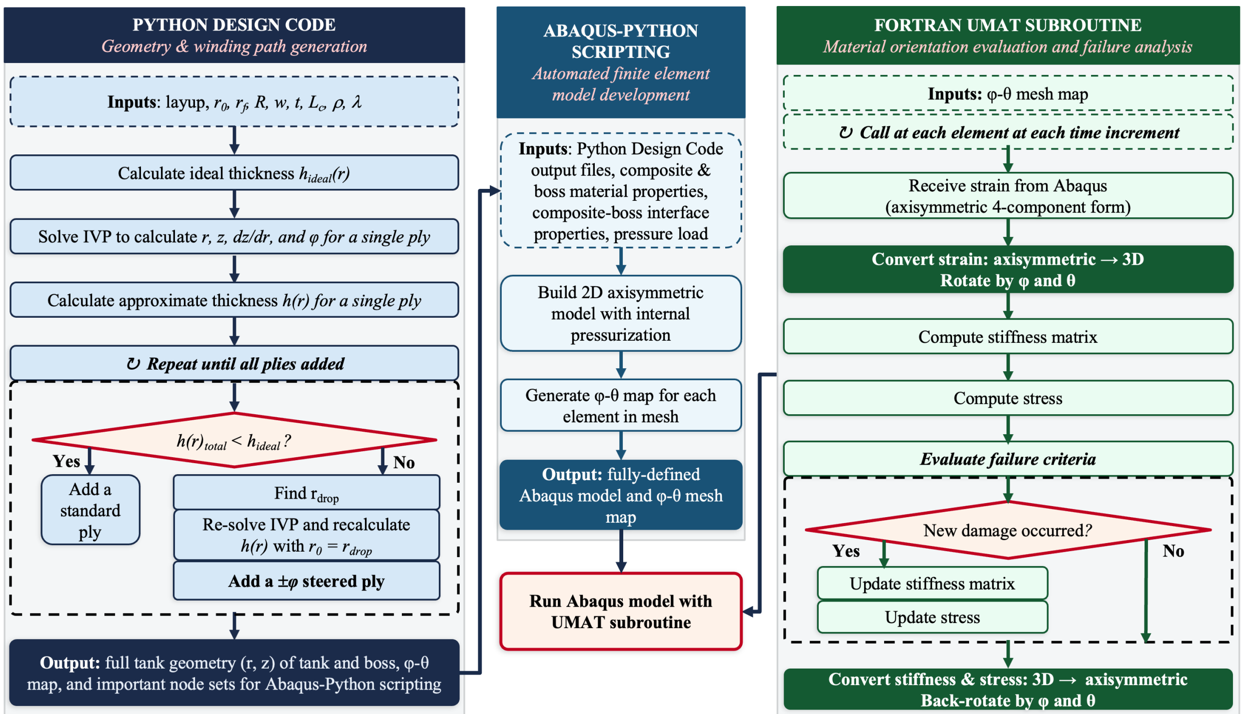

Figure 2. Computational design framework, integrating a Python design code, Abaqus-Python script and Fortran UMAT subroutine.

Operating within an automated workflow, the Abaqus-Python script takes the outputs from the Python design code, along with boss and composite material properties, to construct a 2D axisymmetric finite element model under pressure loading. During execution, the script uses SciPy's cKDTree function as a rapid nearest neighbour lookup tool to find the corresponding φ and θ for each element in the mesh based on the element's centroid. At the beginning of the simulation, the UMAT subroutine reads the resulting φ–θ mesh map once and uses it to evaluate the material response at every integration point and load increment. The subroutine receives the strain tensor from the axisymmetric element in a four-component form, converts it to a 3D representation, and rotates it into the ply material frame by φ and θ. The stiffness matrix and stress are then computed before the failure criteria are applied. If damage is detected, the stiffness matrix is progressively degraded. Finally, the stress and stiffness matrix are back-rotated and converted back to the axisymmetric four-component frame before being returned to the Abaqus solver.

The design-to-analysis framework was used to develop and evaluate two distinct configurations: a validation model and an application model, as shown in Table 1. The validation model replicated the structural simulation from Air et al. [5], applying an internal pressure of 5 MPa to a non-geodesic wound dome with a slippage coefficient $\lambda = -0.2$ and Park Aerospace HTS45E23/E-752-LT material. This model achieved the best performance factor across volume, mass, and Tsai-Wu index among all slippage coefficient iterations. Air et al. [5] reported that both the negative sign and an increased magnitude of the slippage coefficient lead to a better performance factor. These factors drive the trajectory toward higher fibre angles, shifting the orientation closer to the hoop direction and enhancing the tank's hoop stress capacity.

In the work of Air et al. [5], a $\lambda = -0.2$ non-geodesic design was wound over an existing geodesic mandrel. The tank was then hydrostatically pressurized up to 3 MPa, followed by holds at 1.0, 1.5, 2.0, and 3.0 MPa with no leakage recorded. Strain gauge measurements were used to compare the structural simulation results with the physical tank. This comparison revealed deviations of 11.55% and 105.62% between the numerical model and experimental data for maximum and minimum principal strains, respectively. They attributed these differences to observed manufacturing defects in the tank, motivating them to reduce the material stiffness properties E_1 and E_2 by 12% in their simulation. This value is in line with the 10 to 20% stiffness reduction recommended in other studies [14, 15]. The reduced material properties caused the simulation results to have average differences of 1.61% and 18.21% from experimental data. Finally, the material placement and thickness were verified using 3D scanning, with an average difference between analytical and measured results of 1.86 % and 3.45 %, respectively [5].

The application model explored a new design for hydrogen storage at an internal pressure of 20 MPa. A slippage coefficient of $\lambda = -0.2$ was used based on the steering radius limits of the AFP machine, which Air et al. [5] reported as the lower operational limit of their machine. Although IM7/977-3 is not formulated for AFP manufacturing in the same way that HTS45E23/E-752-LT is, it was selected to explore the use of a different material in the design code. In addition, IM7/977-3 has a wide range of material properties available in the literature, making it suitable for more advanced failure criteria, such as the enhanced LaRC05 criteria [16].

Table 1. Input parameters for the design optimization framework.

Parameter	Validation Model	Application Model
Layup	$[90, \pm\varphi_4, 90, \pm\varphi_2]_s$	$[90_6, \pm\varphi_6, 90_4, \pm\varphi_4, 90_4, \pm\varphi_6, 90_6]_s$
Polar boss opening radius r_0 [mm]	60	60
Polar boss contact radius r_f [mm]	73.48	100
Equatorial radius R [mm]	178	178
Fibre bandwidth w [mm]	25.4	25.4*
Ply thickness t [mm]	0.165	0.1358
Length of cylinder region L_c [mm]	200	200
Composite density ρ [kg/mm^3]	1.490×10^{-6} **	1.596×10^{-6}
Slippage coefficient λ	-0.2	-0.2
Composite material	HTS45E23/E-752-LT	IM7/977-3
Composite material properties reference	[17, 18]	[16]
Boss material	Aluminium 7075	Aluminium 7075
Boss material properties reference	[19]	[19]

* The fibre bandwidth w of IM7/977-3 was assumed to be the same as that of HTS45E23/E-752-LT.

** The composite density ρ of HTS45E23/E-752-LT is referenced from another study using an older version of it [20].

The boss material properties, along with certain composite material properties, including the transverse tensile strength Y_T and the out-of-plane shear strength S_{23}, were not reported in [5] or in the manufacturer's datasheet [17]. Thus, assumed values of Y_T = 55 MPa and S_{23} = 78 MPa were used based on other carbon fibre/epoxy materials [21].

The interface between the boss and composite shell can be represented using a cohesive zone model (CZM) to capture progressive degradation of the bond. Following the experimental setup reported in [5], where the components were bonded using Henkel Hysol EA943NA epoxy adhesive, the cohesive properties were approximated using a similar adhesive, Huntsman Epibond 1590 A/B [18, 22]. The penalty stiffness for modes I, II, and III (K_n^0, K_s^0, K_t^0) are numerical values selected to keep the parts tied initially, and these values were assumed for the model. The maximum traction for modes I, II, and III define damage initialization, and these values were taken from [18, 22]. Finally, the fracture toughness for modes I to III $(G_{IC}, G_{IIC}, G_{IIC})$ and the mixed-mode Benzeggagh-Kenane exponent η define damage evolution with the fracture toughness obtained from [18, 22] and the exponent was assumed to be 2 based on a list of values for different material systems presented in [23]. Table 2 shows the CZM implemented in this model to define the surface-to-surface contact of the boss-composite. For the validation model, the Tsai-Wu failure criteria according to [3] were implemented in the UMAT. For the application model, the 3D Hashin failure criteria were used [24], in addition to the Tsai-Wu failure criteria.

Table 2. Boss-composite interface properties.

Property	Value
Penalty stiffness for modes I to III, (K_n^0, K_s^0, K_t^0) [N/mm³]	(2.5×10⁵, 1×10⁵ ,1×10⁵)
Maximum traction for modes I to III (T_n, T_s, T_t) [MPa]	(50, 25, 25)
Fracture toughness for modes I to III $(G_{IC}, G_{IIC}, G_{IIC})$ [N/mm]	(0.125, 1.5, 1.5)
Benzeggagh-Kenane mixed-mode exponent η	2

4. Results and discussion

4.1. Model validation

During model validation, the Python design code results were compared with the benchmark reported in [5], with the inner tank geometry yielding matching values. However, a notable discrepancy was identified in the thickness optimization algorithm results. The current model found two drop radii at 99.23 mm and 104.06 mm, whereas the benchmark model found only one drop radius at 103.17 mm. By hard-coding the current model to ignore the first ply drop, the resulting thickness profile more closely matched the benchmark. This discrepancy suggests that differing algorithmic constraints were applied during optimization.

The validation FEA results are presented in Figure 3, where the longitudinal stress along the fibre and transverse stress of the current model are compared to those in the benchmark model [5]. The current model exhibits similar stress profiles to the benchmark model, with comparable magnitudes over the cylindrical region. However, there were noticeable deviations over the dome region. These discrepancies are likely driven by differences in the FEA modelling approaches. First, the current model simulates the full tank, whereas the benchmark model simulates a half-tank. Additionally, certain parameters were not specified in [5] and therefore had to be assumed, including the exact boss shape, boss material properties, and specific composite strength values. Modelling iterations also revealed that CZM properties strongly influenced stress distributions, introducing a further source of variance. Finally, the steering of two $\pm\varphi$ plies at drop radii, rather than a single ply, also contributes to the differences. The current model yielded a maximum Tsai-Wu failure index of 0.63, which is comparable to the value of approximately 0.52 reported in [5].

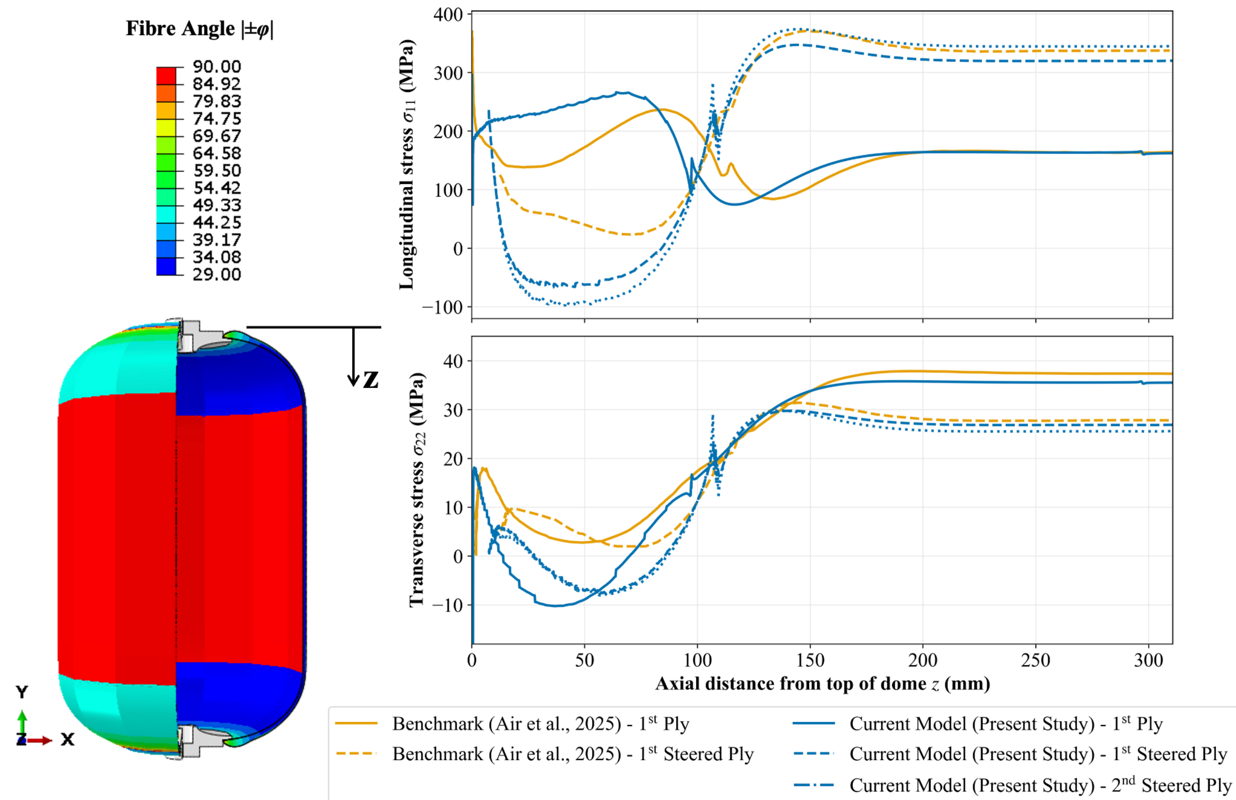

Figure 3. Longitudinal and transverse stresses for the current model and the benchmark model [9], with the 1st ply corresponding to the innermost ±φ ply of the dome region.

4.2. Model application

The design framework was applied to design a tank capable of resisting fibre tensile, fibre compressive, matrix tensile, and matrix compressive failures under a 20 MPa internal pressure. Non-geodesic winding with a slippage coefficient $\lambda = -0.2$, combined with steered plies at each drop radius, results in higher fibre angles that help resist hoop loading in the dome-interface region. The failure indices obtained according to the Hashin failure criteria are presented in Figure 4, with all values remaining below 1, indicating that no failure occurred. The current model predicts high failure indices near the boss-composite interface. However, these values may be unrepresentative of actual physical behaviour, possibly related to the current CZM used for the adhesive bond, given that the dome-cylinder transition region typically yields higher failure indices [5]. Consequently, magnified views of this region are presented, showing maximum failure indices of 0.15 and 0.42 for fibre tension and matrix tension, respectively. To account for the reduced dome volume inherent to the non-geodesic winding paths, the cylinder length of the geodesic design was decreased to establish an equal-volume constraint of 54.5 m^3. Based on this normalization, the optimized non-geodesic configuration achieved a 5.87% composite mass reduction over the geodesic baseline, resulting in an optimized tank mass of 13 kg.

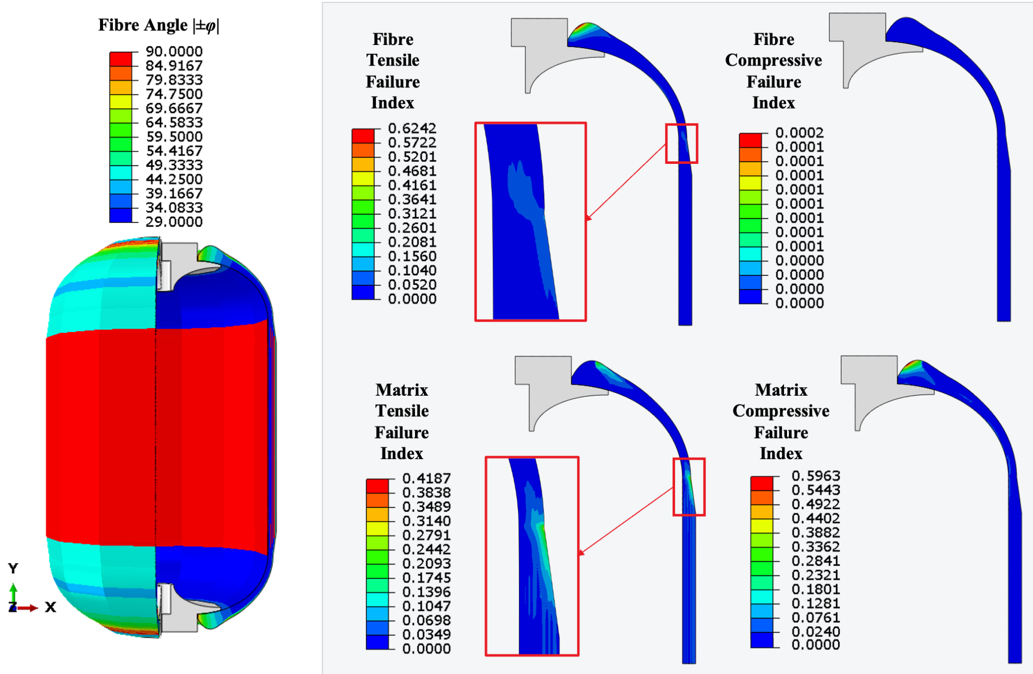

Figure 4. Hashin failure indices of the optimized non-geodesic tank under 20 MPa pressure.

5. Conclusion

AFP manufacturing of Type V pressure vessels offers potential improvements in performance and efficiency for hydrogen composite vessel development. To fully realize these potential benefits, a structured modelling framework is required to enable rapid and efficient design space exploration. Consequently, an automated design-to-analysis tool was developed, integrating three core components: a Python design code to define geometry and winding trajectories according to manufacturing physics, an Abaqus-Python script to automate finite element model generation for tanks under pressure loading, and a Fortran user-material subroutine to model fibre orientations and capture failure. The framework incorporated an optimization algorithm to match tank thickness to the ideal geodesic isotensoid profile by steering plies at selected drop radii based on the methodology described by Air et al. [5]. To validate the tool, a comparative analysis was conducted against the benchmark model presented in [5], using a slippage coefficient of $\lambda = -0.2$ and a pressure of 5 MPa. A separate design was developed at a pressure of 20 MPa to demonstrate the capability of the tool. In future work, the framework will be used to develop designs for higher operating pressures, such as 70 MPa, with the inclusion of appropriate safety factors.

Moving forward, the framework can be refined to address any unexpected modelling results and expanded to include additional capabilities. For example, while the current model features symmetric domes with identical polar bosses at each end, AFP manufacturing, unlike FW, does not require two bosses [2]. The removal of one boss could enable further weight savings, and the Python design code can be extended to include this. Additionally, the code can be updated to leverage AFP's tow-cutting capabilities, allowing for selective ply addition solely in the dome region for local reinforcement. Regarding the FEA, a broader range of materials and CZM properties could also be explored to further enhance analyses. The UMAT can also be upgraded to implement advanced failure criteria, such as the enhanced LaRC05 criteria, to supplement the current Hashin and Tsai-Wu evaluation capabilities. Ultimately, this baseline version of the framework has been developed to enable performance-driven design exploration of AFP-manufactured linerless hydrogen tanks.

6. References

[1] A. Magliano, C. Perez Carrera, C. Pappalardo, D. Guida, and V. Berardi, "A comprehensive literature review on hydrogen tanks: Storage, safety, and structural integrity," *Applied Sciences,* vol. 14, no. 20, 2024.

[2] A. Air, M. Shamsuddoha, and B. G. Prusty, "A review of Type V composite pressure vessels and automated fibre placement based manufacturing," *Composites Part B: Engineering,* vol. 253, p. 110573, 2023.

[3] L. Zu, S. Koussios, and A. Beukers, "Design of filament-wound domes based on continuum theory and non-geodesic roving trajectories," *Composites Part A: Applied Science and Manufacturing*, 2010, vol. 41, 9 ed., pp. 1312-1320.

[4] L. Zu, J. Wang, and S. Li, "Influence of fiber slippage coefficient distributions on the geometry and performance of composite pressure vessels," *Polymer Composites,* vol. 37, no. 1, pp. 315-321, 2016.

[5] A. Air, E. Oromiehie, and B. G. Prusty, "Optimisation of a composite pressure vessel dome using non-geodesic tow paths and automated fibre placement manufacturing," *Composites Part B: Engineering,* vol. 288, p. 111906, 2025.

[6] J. Zhou, J. Chen, Y. Zheng, Z. Wang, and Q. An, "Dome shape optimization of filament-wound composite pressure vessels based on hyperelliptic functions considering both geodesic and non-geodesic winding patterns," *Journal of Composite Materials,* vol. 51, no. 14, pp. 1961-1969, 2017.

[7] M. Leavitt and P. Lam, "Development of advanced manufacturing technologies for low cost hydrogen storage vessels," Quantum Fuel Systems Technologies Worldwide, Inc., Irvine, CA, USA, 2014.

[8] D. A. McCarville, J. C. Guzman, A. K. Dillon, J. R. Jackson, and J. O. Birkland, "Design, manufacture and test of cryotank components," *Comprehensive Composite Materials II*, vol. 3-8, 2018, pp. 153-179.

[9] A. Krikanov, "Refined thickness of filament wound shells," *Science and Engineering of Composite Materials,* vol. 10, no. 4, pp. 241-248, 2002.

[10] V. Vasiliev, A. Krikanov, and A. Razin, "New generation of filament-wound composite pressure vessels for commercial applications," *Composite Structures,* vol. 62, no. 3, pp. 449-459, 2003.

[11] A. Krikanov, "Optimum dome contour of composite shell wound with roving of finite width," *Proceedings of the 2nd Intern. Conference on Composite Science Technology*, 1998, pp. 245-252.

[12] V. Vasiliev, "Composite pressure vessels: analysis, design, and manufacturing," *Bull Ridge Corporation,* 2009.

[13] K. C. Jois, M. Welsh, T. Gries, and J. Sackmann, "Numerical Analysis of Filament Wound Cylindrical Composite Pressure Vessels Accounting for Variable Dome Contour," *Journal of Composites Science,* vol. 5, no. 2, p. 56, 2021.

[14] F. Heinecke, W. van den Brink, and T. Wille, "Assessing the structural response of automated fibre placement composite structures with gaps and overlaps by means of numerical approaches," *Proceedings of the 20th international conference on composite materials*, 2015: Aalborg University Aalborg, Denmark,

[15] K. Fayazbakhsh, M. Arian Nik, D. Pasini, and L. Lessard, "Defect layer method to capture effect of gaps and overlaps in variable stiffness laminates made by Automated Fiber Placement," *Composite Structures,* Article vol. 97, pp. 245-251, 2013.

[16] P. Shabani, L. Li, J. Laliberte, and G. Qi, "Enhanced LaRC05 failure criteria for investigating low-velocity impact on fiber-reinforced composites: An experimental and computational study," *Aerospace Science and Technology,* vol. 155, p. 109554, 2024.

[17] Park Aerospace. " E-752-LT epoxy prepreg." https://parkaerospace.com/wp-content/uploads/2017/04/E-752LT-US-09_21.pdf (Accessed 2026).

[18] A. Air, E. Oromiehie, and B. G. Prusty, "Design and manufacture of a Type V composite pressure vessel using automated fibre placement," *Composites Part B: Engineering,* vol. 266, 2023.

[19] E. Oromiehie, P. Nagulapally, M. J. Donough, and B. G. Prusty, "Automated manufacture and experimentation of composite overwrapped pressure vessel with embedded optical sensor," *International Journal of Hydrogen Energy,* vol. 79, pp. 1215-1226, 2024.

[20] P. T. Maung, B. G. Prusty, M. J. Donough, E. Oromiehie, A. W. Phillips, and N. A. St John, "Automated manufacture of optimised shape-adaptive composite hydrofoils with curvilinear fibre paths for improved bend-twist performance," *Marine Structures,* vol. 87, p. 103327, 2023.

[21] P. D. Soden, M. J. Hinton, and A. S. Kaddour, "Lamina properties, lay-up configurations and loading conditions for a range of fibre-reinforced composite laminates," *Composites Science and Technology,* vol. 58, pp. 1011-1022, 1998.

[22] C. V. Katsiropoulos, A. N. Chamos, K. I. Tserpes, and S. G. Pantelakis, "Fracture toughness and shear behavior of composite bonded joints based on a novel aerospace adhesive," *Composites Part B: Engineering,* Article vol. 43, no. 2, pp. 240-248, 2012.

[23] S. Reddy and K. Shivakumar, "Limited Input Benzeggagh and Kenane delamination failure criterion for mixed-mode loaded fiber reinforced composite laminates," *International Journal of Fracture,* vol. 222, 2020.

[24] J. Gu and P. Chen, "Some modifications of Hashin's failure criteria for unidirectional composite materials," *Composite Structures,* vol. 182, pp. 143-152, 2017/12/15/ 2017.